

# Metal–Organic Framework Mediated Radio-Enhancement Assessed in High-Throughput-Compatible 3D Tumor Spheroid Co-Cultures

Anna Lena Neuer, Alexandra Vogel, Alexander Gogos, Vera M. Kissling, Elena Tsolaki, and Inge K. Herrmann\*

Inorganic nanomaterials have gained increasing attention in radiation oncology, owing to their radiation therapy enhancing properties. To accelerate candidate material selection and overcome the disconnect between conventional 2D cell culture and in vivo findings, screening platforms unifying high-throughput with physiologically relevant endpoint analysis based on 3D in vitro models are promising. Here, a 3D tumor spheroid co-culture model based on cancerous and healthy human cells is presented for the concurrent assessment of radio-enhancement efficacy, toxicity, and intratissural biodistribution with full ultrastructural context of radioenhancer candidate materials. Its potential for rapid candidate materials screening is showcased based on the example of nano-sized metal–organic frameworks (nMOFs) and direct benchmarking against gold nanoparticles (the current “gold standard”). Dose enhancement factors (DEFs) ranging between 1.4 and 1.8 are measured for Hf-, Ti-, TiZr-, and Au-based materials in 3D tissues and are overall lower than in 2D cell cultures, where DEF values exceeding 2 are found. In summary, the presented co-cultured tumor spheroid—healthy fibroblast model with tissue-like characteristics may serve as high-throughput platform enabling rapid, cell line-specific endpoint analysis for therapeutic efficacy and toxicity assessment, as well as accelerated radio-enhancer candidate screening.

## 1. Introduction

Radiotherapy remains a key pillar in cancer therapy, and is often applied in combination with other treatment modalities, including chemotherapy and surgery.<sup>[1]</sup> However, despite technical advances in radiation delivery, such as sophisticated beam geometries,<sup>[2]</sup> radiotherapy is accompanied by significant side effects. Ionizing radiation toxicity to normal tissue typically determines and limits the maximum dose that can be applied to a tumor. As tumors may develop radio-resistance, for example, due to the presence of hypoxia in the tumor center,<sup>[1,3]</sup> novel strategies to render the tumor tissue more susceptible to radiation are in high demand. Amongst other potential strategies, nanoparticle radio enhancement has gained considerable attention in recent years.<sup>[4]</sup> Deposition of metal-containing nanoparticles in tumor tissue has been shown to increase the dose deposition and radiation damage in tumor

tissue more than two decades ago for the first time.<sup>[5]</sup> Experimental evidence has further cemented the promising prospects of nanoparticle radio-enhancement over the years in additional preclinical as well as clinical studies, including the most recent studies on AGuIX in clinical phase I-II, NBTXR3 in clinical phase I-III, and Ferumoxytol in clinical phase I (information obtained from clinicaltrial.gov).<sup>[6]</sup> Despite these encouraging results, the rational design, appropriate material selection, and translation of radio-enhancer candidate materials with maximum therapeutic ratio (high therapeutic efficacy and low intrinsic tissue toxicity) to clinics remains challenging.

To achieve a rational, data-driven radio-enhancer design and development, the screening of large amounts of parameters (e.g., material compositions, particle sizes, concentrations, cell lines, and irradiation conditions) in a high-throughput manner is required. However, current methods based on 2D cell cultures using clonogenic assays are extremely laborious, do not take into account tissue-like features and lack the capability of a concurrent assessment of the normal tissue toxicity.<sup>[7]</sup> The increasing push for the reduction of animal testing in research and the limited physiological meaningfulness of 2D cell cultures call for the

A. L. Neuer, A. Vogel, A. Gogos, V. M. Kissling, E. Tsolaki, I. K. Herrmann  
Laboratory for Particles-Biology Interactions  
Department of Materials Meet Life  
Swiss Federal Laboratories for Materials Science and Technology (Empa)  
Lerchenfeldstrasse 5, 9014 St. Gallen, Switzerland  
E-mail: ingeh@ethz.ch

A. L. Neuer, A. Gogos, E. Tsolaki, I. K. Herrmann  
Nanoparticle Systems Engineering Laboratory  
Institute of Process Engineering  
Department of Mechanical and Process Engineering  
ETH Zurich  
Sonneggstrasse 3, 8092 Zurich, Switzerland



The ORCID identification number(s) for the author(s) of this article can be found under <https://doi.org/10.1002/adbi.202300075>

© 2023 The Authors. Advanced Biology published by Wiley-VCH GmbH. This is an open access article under the terms of the Creative Commons Attribution-NonCommercial License, which permits use, distribution and reproduction in any medium, provided the original work is properly cited and is not used for commercial purposes.

DOI: 10.1002/adbi.202300075

development of advanced in vitro 3D models,<sup>[8,9]</sup> unifying physiological relevance with high-throughput capacity. Additionally, a more in-depth understanding of the cellular fate and toxicity of emerging classes of materials is urgently needed. As 2D cell cultures typically only offer a limited observation window of a few days before cells are overgrowing, 3D spheroid cultures with tissue-like characteristics,<sup>[10–14]</sup> including a distinctly higher radio-resistance in comparison to conventional 2D cell culture<sup>[15,16]</sup> may offer an intermediate step for toxicity evaluation prior to in vivo animal studies. It is increasingly recognized that 3D cultures have the potential to bridge between conventional 2D cell culture, in vivo models and translation into clinics.<sup>[17,18]</sup> Nonetheless, 2D cultures hold many advantages compared to the 3D counterparts, including high controllability, easy repeatability, inexpensiveness and diverse applicability, however, lack tissue mimicry. In particular, the tumor microenvironment is a complex composition of cells, including cancer cells, healthy cells and immune cells, but also extracellular matrix proteins and other macromolecules.<sup>[19–21]</sup> To better mimic physiological tumor characteristics, a variety of 3D models have been proposed previously,<sup>[22–25]</sup> including spheroids, organoids, and (multi)-organ-on-a-chip models, serving as platforms for drug screening or mechanistic studies. Organoids are generally patient tissue-derived and therefore exhibit higher inter-tissue variability, adding another layer of complexity to a platform intended for candidate materials selection. Here, we therefore focus on cell-line-derived spheroids for reasons of standardization. Spheroids can be categorized by the number of different cell types and are either mono-cultured (one cell type) or co-cultured (two or more cell types). Co-cultured spheroids and organoids typically require a cell type-specific endpoint assessment,<sup>[26]</sup> and therefore, co-cultured systems are typically analyzed as labelled single cell suspensions, requiring laborious post-processing, holding the disadvantage of lack in scalability.<sup>[26]</sup> Additionally, spheroids can be distinguished based on the generation technique, including scaffold-free, scaffold-based, agitation-based, or bioprinting methods.<sup>[27]</sup> Scaffold-free methods have the advantage to be highly controllable, relatively low in price and scalable for high throughput screening<sup>[22]</sup> in contrast to scaffold-based methods were the introduced natural or synthetic scaffold may affect the cellular response.<sup>[28]</sup> The right choice of 3D model for the given research question is therefore indispensable.<sup>[19,20]</sup> For radio-enhancer candidate materials selection, a model accounting for tumor characteristics as well as healthy cell surroundings (and radiotoxicity to healthy cells) is most appealing.<sup>[29]</sup> In addition to the biochemical endpoints, a thorough understanding of the nanomaterial uptake and intratissural and intracellular distribution is imperative for candidate materials selection. First steps towards this direction have recently been undertaken by whole slide correlative histology and label-free scanning electron microscopy analysis of spheroids exposed to nanomaterials revealing the nanomaterial distribution within the tissue cross-section, however, lacking ultrastructural context.<sup>[30]</sup>

In this study, we developed an advanced co-cultured human tumor spheroid–healthy fibroblast model featuring key properties of tumor tissue and healthy cell surroundings, as platform enabling rapid, potential high-throughput assessment (compared to conventional assays) of nano-sized radio-enhancer (nRE) candidate materials with regard to therapeutic ratio and cellular fate.

The model offers cell line-specific endpoint analysis compatible with automation<sup>[31]</sup> and high throughput compatibility by reducing post-processing<sup>[26]</sup> (not requiring dissociation in to single cells, labelling, etc. for endpoint assessment). Importantly, the efficacy and toxicity endpoints can be directly related to the nanomaterial uptake and distribution within the spheroids with full ultrastructural context accessible by correlative microscopy. We then showcase the potential of this co-culture model in the concurrent assessment of the radio-enhancement performance and normal tissue toxicity of nano-sized group IV metal–organic frameworks (nanoMOF) with direct benchmarking against gold nanoparticles considered the “gold standard material” for the past two decades in radio-enhancement research.<sup>[5]</sup>

## 2. Results and Discussion

### 2.1. Co-Culture Model Development for Radio-Enhancer Candidate Materials Screening

First, we developed a scaffold free human soft tissue sarcoma tumor spheroid–normal dermal fibroblast co-cultured model, which enables the simultaneous assessment of radio-enhancement and normal tissue toxicity in a high-throughput-compatible manner (**Figure 1**). Tumor cell spheroids of human fibrosarcoma (HT1080) cells were assembled and cultured in the bottom compartment of low-attachment cell culture plates. Non-cancerous human dermal fibroblasts (NHDF) were cultured on polycarbonate trans-well (TW) insert membranes in the top compartment (**Figure 1A**). The seeding density (200–5000 cells) as well as culturing conditions were optimized for spheroid stability and reproducibility. Best results were achieved for 1000 HT1080 seeded on 1% agarose coated 96-well plates in 20% serum-containing culture medium, yielding spherical cohesive microtissues exhibiting linear tissue growth behavior over time. This model further enables straightforward administration of nano-sized radioenhancer (nRE) candidate materials in a controllable manner to the cancerous tumor spheroids. A uniform distribution of nRE within the spheroid can be achieved by nRE treatment prior to tissue formation<sup>[30]</sup> to more closely mimic the expected nanomaterial distribution within tumor tissue in vivo. nRE candidate material administration after tissue formation is likewise feasible; however, nanomaterial tissue penetration in this case has been shown to be limited, and nanomaterials only accumulate in the outermost cell layer of the non-vascularized tumor spheroid—at least for the case of gold nanoparticles and HeLa microtissues.<sup>[30]</sup> Nevertheless, the co-culture model offers high flexibility and freedom in the choice of intratissural nanomaterial distribution (uniform within the tissue, only in the outermost layer, or only in the core).

Based on our spheroid co-culture model, the therapeutic efficacy and toxicity of nRE can be assessed in a straightforward, quantitative, and high-throughput manner. Importantly, the two cell types, the cancerous human sarcoma cells and the healthy human fibroblasts, can be co-cultured for the full duration of the radiation experiment and only separated for the endpoint assessment using a metabolic activity assay, which is less laborious compared to routinely used clonogenic assays. Metabolic activity assays have previously been shown to be equally suitable for endpoint assessment as clonogenic assays;<sup>[32]</sup> in turn,

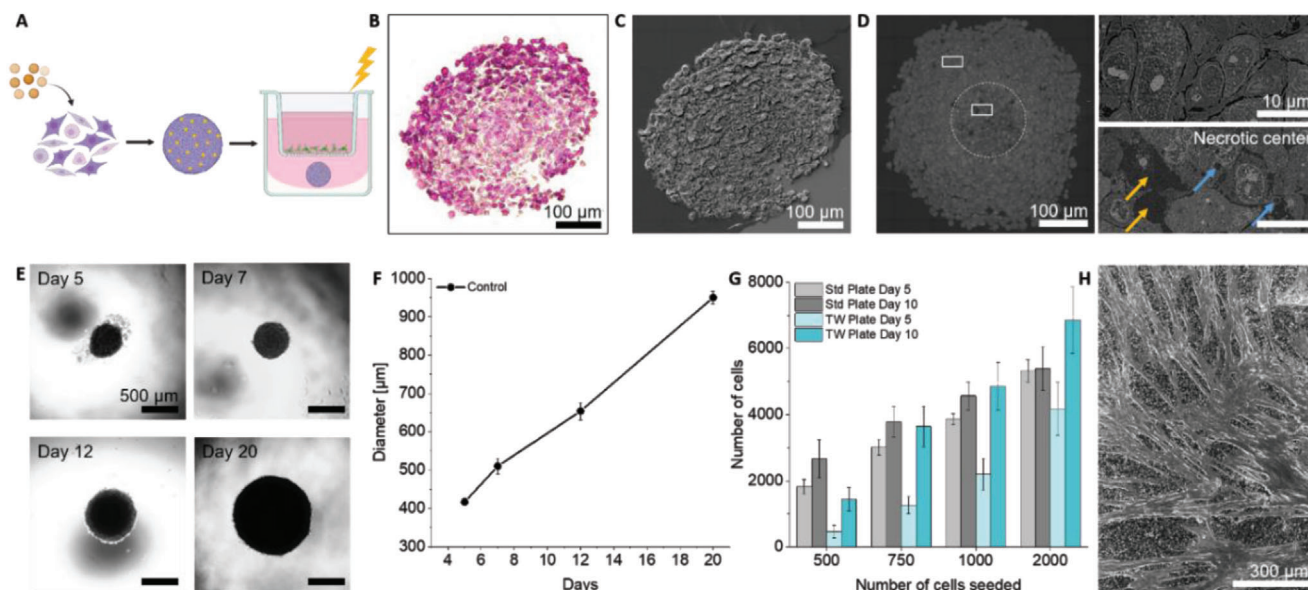


**Figure 1.** Tumor spheroid-normal fibroblast co-culture model development. A) Schematic representation of high-throughput co-culture model. Nano-sized radio-enhancers (nRE, orange) were administered to cancerous human sarcoma cells followed by spheroid formation in agarose-coated low attachment round-bottom plate allowing homogeneous nRE distribution within the spheroid. Non-cancerous fibroblast monolayer (green) on trans-well insert accounts for collateral healthy tissue damage. B) Representative HE stained optical micrograph of an nRE-free tumor spheroid (5  $\mu$ m histology section) and C) the correlative secondary electron scanning electron microscopy (SEM) image of the exact same section. D) Corresponding backscattering electron SEM imaging with ultrastructural cellular context of a 200-nm Epoxy-embedded and Osmium-stained thin section, including zoom-in of tissue (top panel) and necrotic center area (bottom panel) with dead or dying cells, as well as enlarged extracellular space (orange arrow)<sup>[34]</sup> and cytoplasmic vacuoles (blue arrow). Necrotic center is indicated with dashed line. The growth behavior of the tumor spheroids was assessed with E) bright field imaging and F) mean tumor spheroid diameter assessment of at least eight spheroids per condition over a time period of 20 days exhibiting linear growth behavior ( $N = 8$  spheroids per experiment, representative data of  $n = 3$  independent experiments). G) Viability of fibroblast layer assessed by comparison of cell number expansion over time in conventional cell culture plates (Std Plate) and on trans-well inserts (TW Plate) shows comparable growth trends ( $N = 6$  samples per experiment, representative data of  $n = 2$  independent experiments). H) Representative secondary electron SEM imaging of fibroblast layer (2000 cells 5 days after seeding) on trans-well insert. Values in (F) and (G) are displayed as mean with standard deviation.

are significantly less labor-intensive and enable high-throughput analysis and candidate material screening. While cell-line specific endpoint assessment is in principle also possible by flow cytometry, our co-culture model based on inserts does not require preparation of single cell suspensions, which again is laborious, and the metabolic assays based on luminescence are less prone to optical interference with nRE candidate materials. Moreover, the spheroid model development can be characterized and optimized based on correlative light and electron microscopy (CLEM) based on HE-stained (Hematoxylin and Eosin) bright field (Figure 1B) and whole slide scanning electron microscopy (WS-SEM) (Figure 1C) imaging of 5  $\mu$ m histology sections and the direct assessment of nanomaterial distribution within the tissue. The characterization of microtissues using CLEM indicates tissue cohesion and tight cell-to-cell contact, similar to what is observed in actual tumor tissue.<sup>[33]</sup> To assess intratissural nRE distribution and intracellular ultrastructure, tissues are imaged by whole section scanning electron microscopy using 200 nm thin osmium-stained spheroid sections on glassy carbon discs (Figure 1D).

A necrotic center (Figure 1D, dashed line), caused by limitations in nutrient and oxygen penetration (similar to what is observed in actual tumors<sup>[35]</sup>) is observed in spheroids with diameters > 250  $\mu$ m.<sup>[34,36,37]</sup> Additionally, whole section SEM imaging of 200 nm thin sections enables imaging of a large field of view

along with well-preserved ultrastructural imaging. A difference in cell–cell contact between the peripheral region and the necrotic center is visible with tightly packed cells in the peripheral tissue area and loose cell-cell contact, dead, or dying cells and more extracellular space between the cells (Figure 1D, orange arrows) in the spheroid center. The spheroid center shows features characteristic of necrotic and non-dividing cells,<sup>[34]</sup> such as enlarged cytoplasmic vacuoles indicating autophagy (Figure 1D, blue arrows)<sup>[38]</sup> due to oxygen depletion and the presence of dead cells. Spheroid formation and growth can be readily assessed by optical microscopy (Figure 1E,F), again confirming strong cell-cell contact and tissue cohesion from day 7 after seeding and almost linear growth behavior up to day 20. The intactness and viability of the fibroblast layer was quantitatively assessed by metabolic activity measurements based on ATP (Figure 1G) and SEM imaging of the NHDF cell layer on TW inserts (Figure 1H).

## 2.2. Nano-Sized Radio-Enhancer Candidate Materials

To demonstrate the performance of our co-culture model, we investigated the radio-enhancement properties of a selection of group IV nanoMOFs, which are promising radio-enhancers candidate materials,<sup>[39]</sup> in direct comparison to commercially available 50-nm gold nanoparticles, which are the current

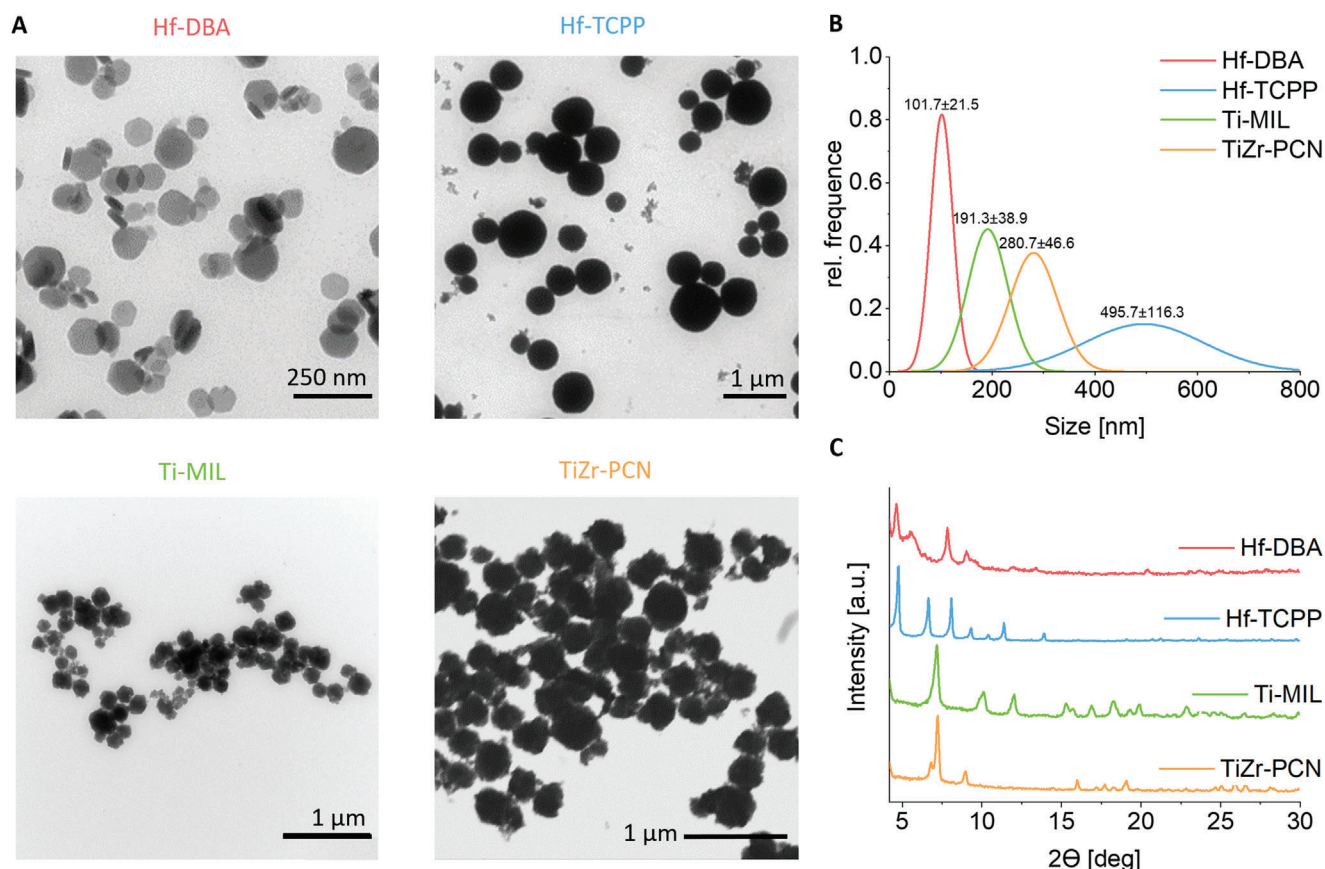


**Figure 2.** Physicochemical characterization of Group IV nano-sized metal–organic frameworks with A) scanning transmission electron microscopy (STEM) imaging, B) normal Gaussian size distribution assessed from STEM imaging ( $N > 80$ ), and C) crystallinity measurement with powder X-ray diffraction. Representative STEM micrographs shown in (A).

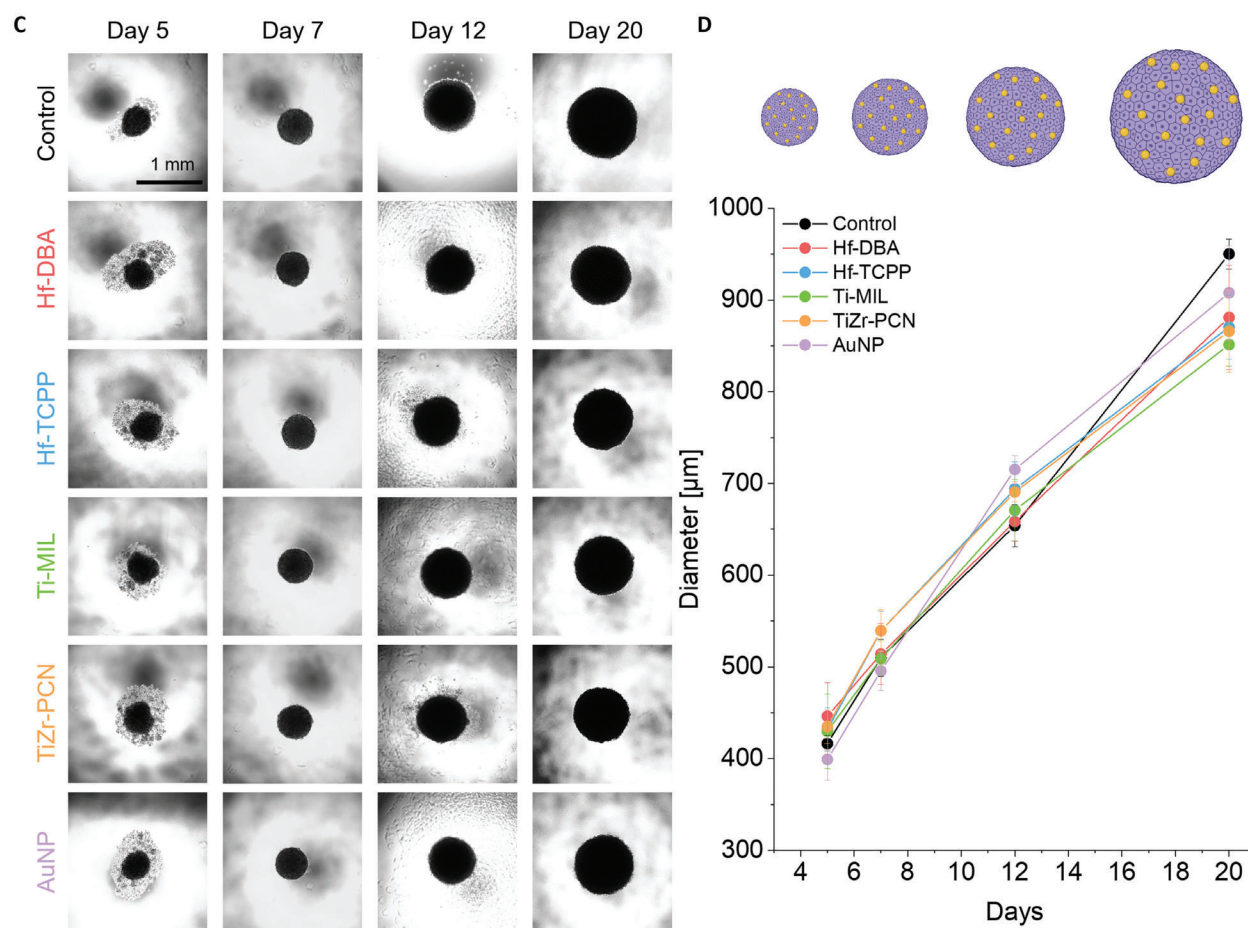
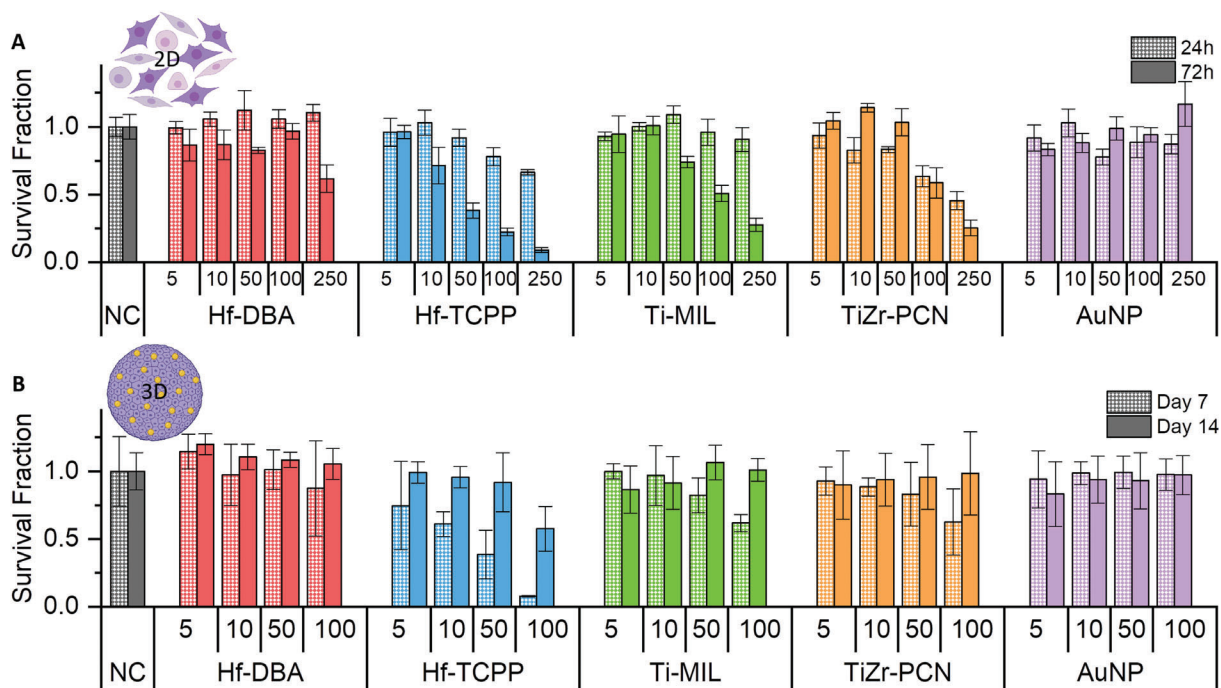
gold-standard material for radio-enhancement in 2D and 3D.<sup>[5,30]</sup> Group IV nanoMOFs, including the high-Z Hf-containing Hf-DBA and Hf-TCPP, as well as the lower-Z Ti-containing Ti-MIL and TiZr-PCN, exhibited primary particle sizes in the range from 100 to 500 nm for their average diameter (Figure 2A,B, also see Figure S1, Supporting Information for histogram size distribution), with Hf-DBA being the smallest with  $101 \pm 22$  nm, followed by Ti-MIL with  $191 \pm 39$  nm, and TiZr-PCN with  $281 \pm 47$  nm, and Hf-TCPP being the largest with  $496 \pm 116$  nm. Ti-based nanoMOFs have recently been shown to exhibit particularly promising radio-enhancement properties in 2D cell cultures with dose enhancement factors reaching up to three, even outperforming higher-Z Hf-containing nanoMOF materials.<sup>[39]</sup> Powder X-ray diffraction confirmed high crystallinity for all nanoMOFs (Figure 2C). A comprehensive analytical characterization of these nanoMOF materials is available elsewhere.<sup>[39]</sup>

### 2.3. 2D and 3D nRE Biocompatibility and Influence on Tumor Spheroid Growth

Initially, nRE biocompatibility (Figure 3) was assessed in the 2D cell culture of HT1080 cells (Figure 3A) and fibroblasts (Figure S2, Supporting Information), as well as the HT1080 3D tumor spheroid model (Figure 3B). The application of nRE is exclu-

sively targeted to tumors to maximize the therapeutic ratio, and with the previously described setup nRE are exclusively applied to tumor spheroids. Nonetheless, the biocompatibility of nRE toward NHDF was assessed to avoid potential adverse effects. In the 2D HT1080 cell culture and particle doses up to  $250 \mu\text{g mL}^{-1}$ , a dose-dependent viability reduction was found for all nRE with the exception of Hf-DBA and AuNP with no compromised viability (Figure 3A) after 24 h short-term and only minor viability reduction for Hf-DBA after 72 h long-term endpoint analysis.

All nREs were well tolerated in normal human fibroblasts with no detectable viability reduction up to  $250 \mu\text{g mL}^{-1}$  particle treatment concentrations (Figure S2, Supporting Information). Tumor spheroids exhibited higher tolerance towards nRE candidate materials in comparison to 2D HT1080 cells, with almost no or only minor changes in viability at Day 7 and no compromised viability at Day 14 after spheroid formation, with an exception for Hf-TCPP, where an evident dose-dependent reduction below 10% viability was detected at a concentration of  $100 \mu\text{g mL}^{-1}$  after 7 days with a slight recovery in the viability after 14 days (Figure 3B). The transient nature of the viability reduction effect was observed after 14 days in comparison to 7 days after nRE treatment for Hf-TCPP, and to a lesser extent also for Ti-MIL and TiZr-PCN. This may be attributed to a higher nutrient and oxygen concentration at the inner layers of the spheroid after nRE-mediated toxicity-induced cell death, and the therefore



subsequent size reduction, resulting in faster re-proliferation. Nutrients, as well as oxygen, become greatly limited in spheroids with diameters exceeding 250  $\mu\text{m}$ ,<sup>[36,37]</sup> which is a size purposefully aimed at in this model for characteristic hypoxic tumor mimicry. In summary, all nRE exhibited high biocompatibility over 2 weeks of tumor spheroid cultivation with up to 100  $\mu\text{g mL}^{-1}$  nRE treatment except for Hf-TCPP. In accordance with the biocompatibility assessment, sub-toxic treatment doses were defined as 50  $\mu\text{g mL}^{-1}$  for Hf-DBA, Ti-MIL, TiZr-PCN, and AuNP, and 5  $\mu\text{g mL}^{-1}$  for Hf-TCPP. Furthermore, we assessed nRE-dependent growth behavior (Figure 3C,D) of tumor spheroids over 20 days using light microscopy. We measured the diameter of at least eight spheroids per condition and found a remarkably comparable and nearly linear growth behavior for sub-toxic nRE treatment doses in the absence of radiation.

#### 2.4. Nano-Sized Radio-Enhancer Uptake and Intratissural Distribution

Following biocompatibility investigations, we assessed the uptake and intratissural distribution behavior of the sub-toxic nRE exposure eight days after spheroid formation (Figure 4). Figure 4A shows the metal mass per spheroid, determined using inductively coupled optical emission spectroscopy (ICP-OES), compared to the total particle mass per spheroid to set the differences of the metal-organic composite nanoMOF nRE in relation to solid gold nanoparticles. This is used to reliably interpret efficiencies in later irradiation experiments. The total particle mass for nanoMOFs was calculated by the metal fraction determined using ICP-OES.<sup>[39]</sup> For the metal mass in nanograms per spheroid, nanoMOF treated spheroids have a 3–10-fold lower metal mass load in comparison to AuNP. In turn, the theoretical particle masses of Hf-TCPP, Ti-MIL, TiZr-PCN, and AuNP are  $1076 \pm 6$ ,  $1399 \pm 24$ ,  $1714 \pm 43$ , and  $1256 \pm 1$  ng spheroid<sup>-1</sup>, respectively, for the higher 50  $\mu\text{g mL}^{-1}$  treatment concentration, which is in the same order of magnitude. In this setting, only Hf-DBA showed a lower particle mass uptake with  $355 \pm 8$  ng spheroid<sup>-1</sup> for the higher treatment concentrations of 50  $\mu\text{g mL}^{-1}$ . These results are in good agreement with previously shown uptake experiments performed in 2D cell culture with similar uptake trends and absolute uptake in the same order of magnitude (ng spheroid<sup>-1</sup> corresponds to pg cell<sup>-1</sup>).<sup>[39]</sup> SEM imaging of 200-nm-thin sections (Figure 4B) of tumor spheroids treated with sub-toxic nRE doses revealed a homogeneous nRE distribution across tissue sections. The spheroid cross-sections (Figure 4B-I, left panel) also showed the tumor tissue characteristic necrotic core for all nRE-treated and untreated spheroids (Figures 4B and 1D).

The different diameters of the necrotic core are attributed to differences in the sectioning planes. Arrows in the Figure 4B-

II panel (middle-left) highlight particles across the tissue at a comparatively large field of view, whereas the Figure 4B-III panel (middle-right) displays the particles found in membrane-bound vesicles with almost single-particle resolution. Density-dependent color SEM (Figure 4B-IV right panel) enables clear distinction of the higher electron density of all nRE compared to biological tissue for even better contrast and separation between biological matter and metal based nRE. The homogeneous distribution of nRE within the tumor tissue did not alter the cellular morphology, once more confirming the good biocompatibility of nRE at the selected treatment dose in the absence of ionizing radiation.

#### 2.5. nRE-Based Radio-Enhancement, Normal Tissue Toxicity and Therapeutic Ratio

After successful development of the co-cultured in vitro tumor spheroid and healthy fibroblasts model, we assessed the radio-enhancement efficacy (Figure 5) in a 150 keV X-ray irradiation experimental setup. Tumor cells were treated with nRE at sub-toxic concentrations of 50  $\mu\text{g mL}^{-1}$  for Hf-DBA, Ti-MIL, and TiZr-PCN, 5  $\mu\text{g mL}^{-1}$  for Hf-TCPP, and 50 and 200  $\mu\text{g mL}^{-1}$  for AuNP for 24 h prior to spheroid formation. Tumor spheroids were irradiated on day 7 after tissue formation. NHDF cells on TW inserts were joined with spheroids on the day of irradiation and maintained in co-culture for the entire duration of the experiment. Hence, the effect of ionizing radiation was studied in combination with nRE solely applied to cancerous cells in a joint system with healthy fibroblasts. The assessment of 3D tumor spheroid and fibroblasts on TW insert survival fractions (Figure 5A) and bright field imaging of 3D tumor spheroids (Figure 5C) was performed on day 8 after irradiation (Day 15 after spheroid formation), revealing a clear radio-enhancement effect for all nRE. Figure 5B shows dose enhancement factors at 4 Gy irradiation ( $\text{DEF}_{4\text{Gy}}$ ), dose modifying ratios at 50% survival ( $\text{DMR}_{50\%}$ ), and lethal dose 50% ( $\text{LD}_{50}$ ) (Table S1, Supporting Information provides detailed data). Hf-TCPP clearly outperformed all tested nRE in terms of their radio-enhancement efficacies with a  $\text{DMR}_{50\%}$  of  $1.47 \pm 0.04$ , as the treatment dose was ten-fold lower compared to the other nanoMOFs and even 40-fold lower than the 200  $\mu\text{g mL}^{-1}$  AuNP treatment. TiZr-PCN performed with a  $\text{DMR}_{50\%}$  of  $1.38 \pm 0.03$  and AuNP (200  $\mu\text{g mL}^{-1}$ ) of  $1.50 \pm 0.03$  similarly well as Hf-TCPP, whereas Hf-DBA, Ti-MIL, and AuNP (50  $\mu\text{g mL}^{-1}$ ) showed a  $\text{DMR}_{50\%}$  of around 1.2 (Table S1, Supporting Information). The 200  $\mu\text{g mL}^{-1}$  treatment concentration of AuNP was included to directly compare the results to previously conducted experiments of AuNP in HeLa spheroids under comparable conditions. Therein, we observed an enhancement effect for 200  $\mu\text{g mL}^{-1}$  AuNPs in a similar range with a radiation enhancement ratio at 4 Gy irradiation ( $\text{RER}_{4\text{Gy}}$ ) of 1.55.<sup>[30]</sup> In the

**Figure 3.** A,B) Nano-sized radio-enhancer (nRE) cytocompatibility towards HT1080 human sarcoma cells in 2D and 3D culture, and C,D) nRE effect on 3D tumor spheroid growth rate. Short- and long-term nanoMOF and AuNP toxicity in A) 2D cell culture for 24 and 72 h with treatment concentrations of 5–250  $\mu\text{g mL}^{-1}$  ( $N = 4$  replicates per experiment,  $n = 3$  independent experiments) and B) 3D tumor spheroids for 7 and 14 days post-seeding for treatment concentrations of 5–100  $\mu\text{g mL}^{-1}$  ( $N = 5$  spheroids per experiment,  $n = 3$  independent experiments) and respective negative control (NC, untreated). nRE effects on the spheroid growth rate for a sub-toxic concentration (50  $\mu\text{g mL}^{-1}$  for Hf-DBA, Ti-MIL, TiZr-PCN, and AuNP and 5  $\mu\text{g mL}^{-1}$  for Hf-TCPP), employed for radio-enhancement investigations, analyzed by C) bright field imaging of one representative spheroid and respective D) mean diameter of eight individual spheroids over a course of 20 days ( $N = 8$  spheroids per experiment,  $n = 3$  independent experiments). Values are displayed as mean with standard deviation.

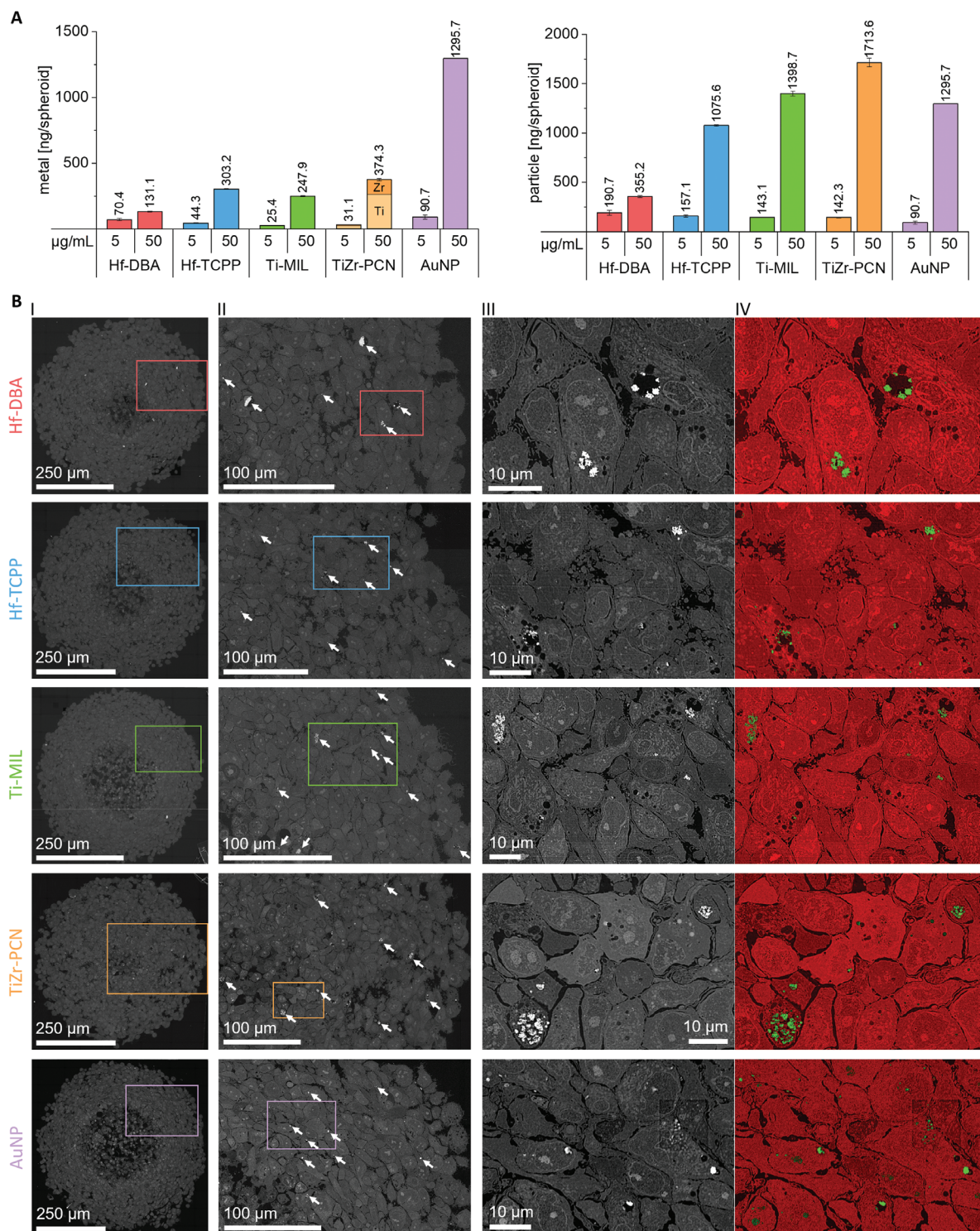


**Figure 4.** Intratissural nRE uptake and distribution. A) Intratissural nRE concentration of eight individual spheroids as mean metal mass (determined using ICP-OES, data above the bars for total metal mass) and total particle mass per spheroid ( $N = 14$  spheroids per experiment). Bars show mean and standard deviation. B) Representative nRE distribution within the spheroid analyzed with SEM backscatter imaging with high resolution imaging of the whole spheroid section (B-I) and higher magnification (B-II/III area indicated by rectangles), as well as density-dependent color imaging (B-IV) of 100–200 nm thin sections with single particle resolution (particles in green). For ICP-OES analysis, cells were incubated with 5 and 50  $\mu\text{g mL}^{-1}$  for all nRE and for SEM analysis, 50  $\mu\text{g mL}^{-1}$  for Hf-DBA, Ti-MIL, TiZr-PCN, and AuNP and 5  $\mu\text{g mL}^{-1}$  for Hf-TCPP over a 24-h period prior tissue formation. Analysis was performed on Day 8 after tissue formation for both ICP-OES and SEM analysis. Representative SEM micrographs shown in (B).

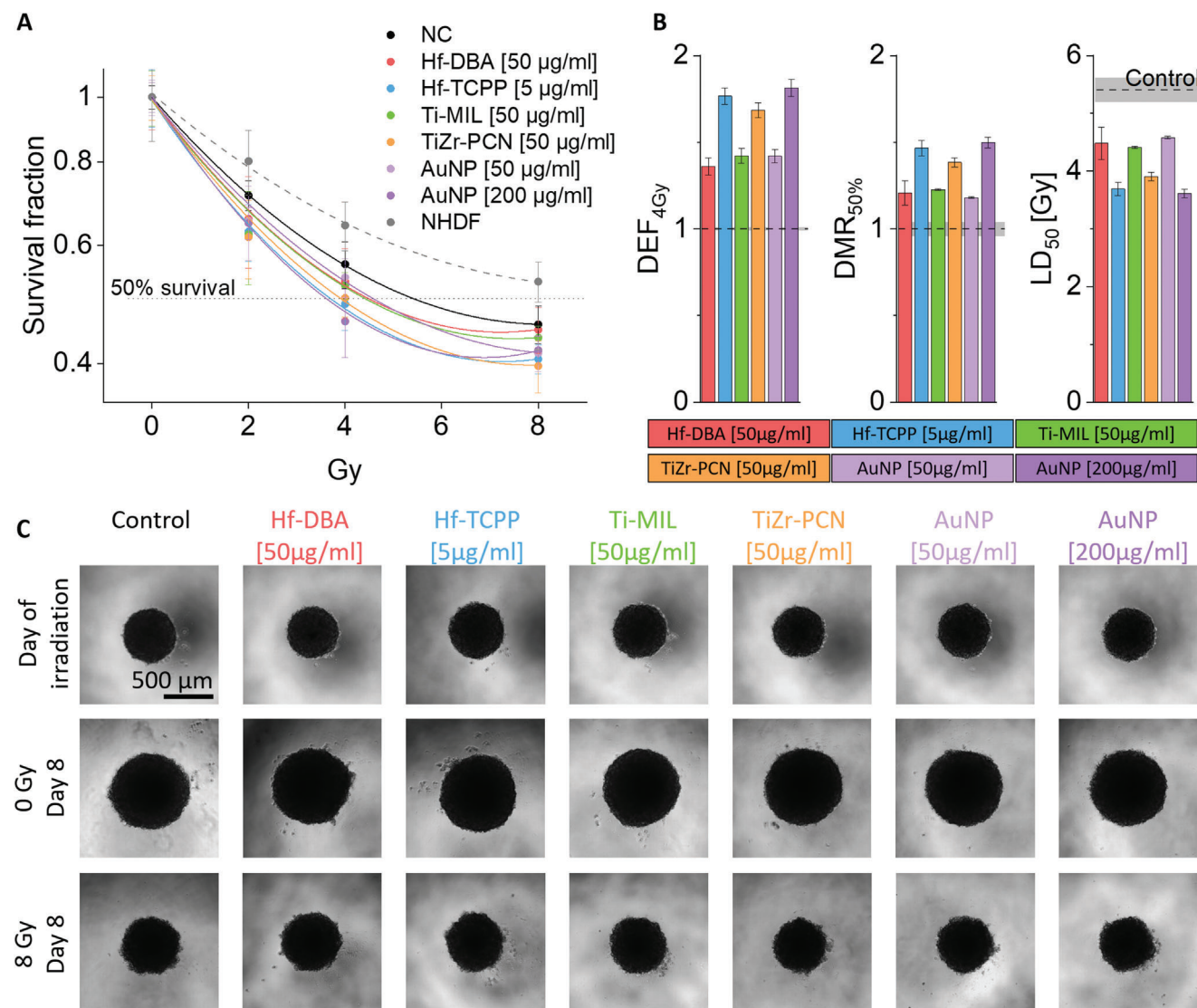


**Figure 5.** Radio-enhancement performance of nRE in co-cultured tumor spheroid. A) Survival fractions of 3D tumor tissues as well as fibroblasts seeded on TW inserts were analyzed 8 days after irradiation (15 days after spheroid formation) dependent on ATP metabolic activity for treatment concentrations of 50  $\mu\text{g mL}^{-1}$  Hf-DBA, Ti-MIL, and TiZr-PCN, 5  $\mu\text{g mL}^{-1}$  Hf-TCPP, and 50 and 200  $\mu\text{g mL}^{-1}$  of AuNP (nRE treatment solely in 3D tissues), NC: negative (untreated) control ( $N = 8$  spheroids per condition,  $n = 3$  independent experiments). B) Radio-enhancement efficacy of individual nREs are given as dose enhancement factors at 4 Gy ( $\text{DEF}_{4\text{Gy}}$ ) irradiation as well as dose modifying ratios at 50% survival ( $\text{DMR}_{50\%}$ ) and  $\text{LD}_{50}$  irradiation dose. Bars show mean and standard deviation. C) Representative brightfield imaging of the tumor spheroid provides visual proof for nRE compatibility in the irradiation free control during the experiment, as well as the radiation effects.

present setting, the  $\text{RER}_{4\text{Gy}}$  for HT1080 spheroids was with 1.22 lower, which is likely due to cell line specific differences. The  $\text{RER}_{4\text{Gy}}$  in a 2D setting for HeLa cells was 2.1,<sup>[30]</sup> whereas in the case of HT1080 cells, it was 1.68 (with exactly the same setting as in Figure S3C,D, Supporting Information), demonstrating the radio-resistant properties of HT1080.<sup>[40]</sup>

In HT1080 cells, 3D spheroids have overall lower radio enhancement effects compared to previously published effects in 2D monolayer scenarios were  $\text{DMR}_{50\%}$  up to 3.8 were found (treatment concentration 40  $\mu\text{g mL}^{-1}$ ).<sup>[39]</sup> Generally, more complex 3D tissues with cell–cell interaction scenarios are believed to have a higher radio-resistance in comparison to 2D monolayer cells without tighter cell–cell interactions.<sup>[41]</sup> This

higher resistance was previously explained, for example, with changes in cell cycle regulation, gene expression, and chromatin density modifications.<sup>[41–44]</sup> Therefore, we directly compared similarly treated, handled, and cultured cells in 2D (Figure S3A,B, Supporting Information) and 3D conditions (Figure 5), as the differences in the culture dish size, treatment method, and handling can tremendously impact the enhancement effect variability. In 2D conditions (Figure S3A–D, Supporting Information), a strong metal-species dependence was observed with Ti-based materials (Ti-MIL and TiZr-PCN) performing best, followed by Hf-based materials (Hf-TCPP and Hf-DBA). Although the enhancement trend was similar in both settings, the overall  $\text{DMR}_{50\%}$  were lower in 96-well plates compared to

48-well plates.<sup>[39]</sup> However, in 3D conditions, this trend was absent. Radiation enhancement with Ti-MIL in 3D cancerous tissues only performed slightly better than Hf-DBA (Figure 5A,B), whereas the uptake of Hf-DBA was three-fold lower in comparison to all other nanoMOFs (Figure 4A). In particular, changes in the Ti-MIL performance in 2D versus 3D were surprising and might be attributed to the oxygen gradient in 3D tumor tissues, due to the strong dependence of the catalytic effect of Ti-MIL on oxygen.<sup>[45]</sup> These distinct differences between the relative enhancement factors for the different candidate materials between 2D and 3D clearly highlight the importance of models exhibiting tissue like properties. The fibroblasts seeded on TW inserts remained well above a 50% survival fraction up to the highest radiation dose applied in this study, demonstrating the lower radiation effect on healthy cells, and preferential radiation damage to nRE-containing tumor tissue. Furthermore, it must be considered that the NHDF cells in this model were grown in 2D, whereas cancerous cells are grown in 3D spheroids, which have, as mentioned before, expectedly higher radio-resistant properties.<sup>[41–44,46]</sup>

### 3. Conclusions

We introduce an advanced in vitro human co-culture model for the straightforward assessment of nanoparticle radio-enhancement and concurrent healthy tissue toxicity in in vivo-mimicking conditions. This advanced in vitro model enables the concurrent assessment of radio-enhancement effects, as well as surrounding healthy tissue damage, in a straightforward and quantitative manner, and within context of nanomaterial uptake and intratissural distribution. Functional analysis of nanoMOF radio-enhancers and benchmarking against gold nanoparticles using this co-culture model illustrates the promising potential and importance of nanoMOF-based radio-enhancer testing in 3D models rather than conventional cell cultures. Dose enhancement effects in the spheroids were overall in a similar range as typically found in vivo and lower than in the 2D cultures.<sup>[47]</sup> We conclude that not only intrinsic material properties of the nRE affect the radio-enhancement performance, but also tissue features not adequately mimicked by 2D cell cultures, including intratissural cell–cell interaction,<sup>[48]</sup> the altered oxygen and nutrient supply,<sup>[16,49–51]</sup> and radio resistance,<sup>[48]</sup> influence the overall outcome. In summary, this advanced co-culture model presents a platform with the possibility for high-throughput nRE testing under tissue-like conditions with the goal to reduce animal testing and contribute to an improved, data-driven selection of radio-enhancers with high therapeutic ratio for radiotherapy, translation into clinics.

### 4. Experimental Section

**Cell Culture:** Cancerous HT1080 (human fibrosarcoma cell line, ATCC, USA) and non-cancerous NHDF (normal human dermal fibroblast primary cells, PromoCell, Germany) were cultured in Minimum Essential Medium Eagle (MEM, Sigma-Aldrich, Germany) supplemented with 10% Fetal Calf Serum (FCS, Sigma-Aldrich, 1% L-Glutamine (Sigma-Aldrich), 1% Penicillin-Streptomycin (PS, Sigma-Aldrich), 1% Non-Essential Amino Acids (NEAA, Sigma-Aldrich), and Dulbecco's Modified Eagle's Medium – high glucose (DMEM, Sigma-Aldrich) supplemented with 10% FCS, 1% L-Glutamine, and 1% PS.

**Co-Culture Tumor Model:** For nRE treatment, 100.000 HT1080 (maximally up to passage 12) cells were seeded in a six-well plate and allowed to attach. They were then treated with the respective nRE concentration for 24 h. Remaining nRE were washed twice with phosphate buffered saline (PBS, Sigma-Aldrich), detached and counted. For the 3D spheroid culture, HT1080 full growth medium supplemented with 20% FCS was used. The desired number of cells was suspended in fresh medium, and 1000 cells spheroid<sup>−1</sup> in 100  $\mu$ L were seeded in a 50  $\mu$ L 1% agarose-coated plate. During spheroid culture, the medium was renewed every 3–4 days by replacing 50  $\mu$ L of medium with fresh medium. Spheroids were transferred to a new 50  $\mu$ L 1% agarose-coated plate on Day 10–12 after formation to ensure stable and healthy growth.

For the co-culture, 1000 NHDF cells in NHDF growth medium were seeded in 75  $\mu$ L on a transwell (TW) insert (HTS Transwell-96 #3386, Corning, USA) with 235  $\mu$ L of the same medium in the lower receiving plate compartment, and allowed to attach overnight before transferring to the spheroid containing plate. For the remaining experimental process, the HT1080 spheroid and NHDF layer on transwell were cultured together with medium exchange in both compartments every 3–4 days.

**Correlative Histology-SEM:** Spheroids were fixed with 2.5% glutaraldehyde (Sigma-Aldrich) in 0.1 M sodium cacodylate buffer for 2 h at room temperature (RT) and overnight at 4 °C. Prior to embedding, 10–15 MT were pooled and pre-embedded in 3% agarose (Sigma-Aldrich). For paraffin embedding, a Myr Spin Tissue Processor STP120 (Tarragona) was used with a total dehydration and paraffin immersion time of 3 h. A Leica Biosystem microtome (Leica Biosystems, Switzerland, RM2235) was used for 5  $\mu$ m sectioning. The sections were transferred onto X-tra (Leica Biosystems) adhesive slides. For Hematoxylin-Eosin (HE) staining, a Slide Stainer MYREVA SS-30 (Tarragona) was used, and sections were covered with ethanol and a coverslip for direct bright field (BF) imaging with a ZEISS Primovert microscope with an Axiocam 105 (Zeiss, Switzerland). The cover slips were gently removed, and samples were air dried before backscattering scanning electron microscopy (SEM) using an Axia ChemiSEM SEM (Thermo Fischer Scientific).

To image NHDF monolayers on TW inserts, cells were fixed as described above. Membranes were air-dried and fixed on a SEM specimen stub with a carbon tape. Before imaging, 10-nm carbon coating was applied using a Leica EM ACE600 (Leica Biosystems) sputtercoater to reduce charging effects.

**High-Resolution Cellular Ultrastructure SEM:** Spheroids were pooled and fixed as described above. Samples were stained with 1% osmium tetroxide in 0.1 M sodium cacodylate buffer for 1 h at RT while protected from light. Three times washing with water for 3 min each was followed by a subsequent dehydration series (30%, 50%, 70%, 90% ethanol for 5 min each, three times 100% ethanol for 10 min each) at RT. Samples were immersed for 1 h in 1:1 epon:ethanol (Epoxy embedding kit, #45 359, Sigma-Aldrich), overnight in pure epon and polymerized in fresh 100% epon at 60 °C for 48 h. Ultrathin sections of 200 nm thickness were cut using an ultramicrotome (Leica Biosystems, EM UC6) and placed on a high purity glassy carbon disc (Tedpella, USA) for ultra-low background imaging, only providing C in EDX analysis. High-resolution images of the spheroids and their cellular ultra-structure were constructed from single tiles using the software Maps 3.19 (Thermo Fisher Scientific). The single image tiles were collected using an Axia ChemiSEM (Thermo Fisher Scientific) using a concentric backscatter detector (CBS) in beam deceleration mode with a stage bias of -4 kV and a landing energy of 4 keV.

**NanoMOF Synthesis and Characterization:** Hf-DBA, Hf-TCPP, Ti-MIL, and TiZr-PCN were synthesized following previously published procedures.<sup>[39]</sup> For scanning transmission electron microscopy (STEM) characterization, 500  $\mu$ L of 0.1 mg mL<sup>−1</sup> particle suspension in ethanol was centrifuged onto copper grids (EMR, Holey Carbon Film 200 Mesh) for 10 min at 21.000  $\times$  g and analyzed with a Hitachi S-4800 (Hitachi) scanning electron microscope. The images were also used for size distribution measurement using the Fiji-ImageJ software (2.1.0/1.53c / Java 1.8.0\_172). X-ray diffraction (XRD) patterns were obtained from dry particle powders measured at diffraction angles 2 $\theta$  from 4° to 30° with a 0.05°

step using a PANalytical X'Pert Pro MPD (Malvern, 40 kV, 40 mA). Citrate-stabilized gold nanoparticles (50 nm) were commercially purchased from nanoComposix (USA, #AUCB50-1 M).

**Viability Assessment:** For viability assessments in 2D and 3D cell culture, a luminescence-based ATP quantification assay (CellTiter-Glo Luminescent Cell Viability Assay, Promega, Switzerland, 2D #G7573 and 3D #G9682) was used.<sup>[52]</sup> Briefly, for the 2D nRE biocompatibility assessment, the desired amount of cells (HT1080 5000 for 24 h, 2000 for 72 h time point; NHDF 8000 for 24 h, 5000 for 72 h time point) were seeded in a conventional black clear-flat-bottom 96-well plates (Greiner #655 090) and allowed to attach overnight, followed by a 24 h nRE treatment under standard culture conditions. Remaining nRE were washed twice with PBS, and cells were either immediately analyzed or further cultured until 72 h after nRE treatment. CellTiter-Glo assay was performed according to the manufacturer protocol with 50  $\mu$ L fresh medium and 50  $\mu$ L reagent. The plate was shaken for 30 min, followed by 10 min signal equilibration in the dark before luminescence determination using a Mithras LB 943 Multimode plate reader.

For NHDF growth behavior on TW inserts, a NHDF standard curve was determined from 200–5000 cells in a black clear-flat-bottom 96-well plates. The assay was conducted as described above, but with 75  $\mu$ L containing the respective number of cells and 75  $\mu$ L reagent as the liquid level adjusted for TW analysis. The number of cells in a conventional plate and on TW inserts were determined five and ten days after seeding (medium exchange every 3–4 days). The TW insert was transferred to a black clear-flat-bottom 96-well plate for comparability reasons, and the membrane was pierced. Prior to luminescence determination, the TW insert was gently removed.

The 3D biocompatibility 3D CellTiter-Glo assay was performed similarly as described above, after the spheroid transfer to a black clear-flat-bottom 96 well plate with 50  $\mu$ L medium containing the spheroid and 50  $\mu$ L reagent. For co-cultured NHDF cells, the TW insert was transferred to a black clear-flat-bottom 96-well plate and continued as described above using the 2D CellTiter-Glo assay.

**Quantitative Intratissural nRE Uptake:** The intratissural nRE elemental uptake was analyzed with inductively coupled plasma optical emission spectroscopy (ICP-OES). Spheroid formation and nRE treatment of 5 and 50  $\mu$ g mL<sup>-1</sup> was performed as described above. For analysis, eight spheroids under the same conditions were pooled in 50  $\mu$ L medium in a quartz tube and prepared with 1500  $\mu$ L sulfuric acid (H<sub>2</sub>SO<sub>4</sub>) and 1500  $\mu$ L ultrapure water. They were allowed to react for 20 min before 1000  $\mu$ L hydrogen peroxide (H<sub>2</sub>O<sub>2</sub>) was added. A pressurized microwave (turboWAVE 1500 MWS GmbH, Germany) at 1000 W, 200 °C, and 150 bar pressure was used during 40 min for digestion. The digestion procedure in comparison to the standard digestion method using hydrofluoric acid was verified in a previous study.<sup>[39]</sup> The digested samples were transferred to 50-mL falcon tubes and filled up to 25 mL with 2% nitric acid (HNO<sub>3</sub>). The elements of interest were then quantified using an Agilent 5110 ICP-OES (Agilent, Switzerland) with an external calibration from 0 to 5 ppm in 2% HNO<sub>3</sub>.

**In Vitro Irradiation Enhancement:** Spheroid formation and nRE treatment was performed as described before. Spheroid formation was allowed for 7 days before 1000 NHDF were seeded on transwell inserts (HTS Transwell-96 #3386, Corning). After being allowed to attach overnight, NHDF were joined with the spheroids and cultured in co-culture during the entire experiment. The HT1080 spheroids and NHDF cells were separated only for medium exchange every 3–4 days. For the entire co-culture period, a compartment-specific culture condition was followed with full-growth MEM containing 20% FCS for spheroids in the bottom compartment and full-growth DMEM containing 10% FCS for NHDF cells in the top compartment. For irradiation on Day 7 after spheroid formation, the co-culture model was transported in a CellTrans 2018 transportable incubator (Labotect, Germany, 37 °C at 5% CO<sub>2</sub> concentration) to the X-ray facility and placed into a 6 cm thick Perspex plate functioning as a water phantom to simulate more reliable physiological conditions.<sup>[53]</sup> Irradiation was performed with a 150 keV SEIFERT X-ray Tubehousing ISOVOLT 420/10 (Seifert) operating at 20 mA equipped with a Thoreaus1 filter, and a 12 mm thick aluminum plate was used for beam hardening. On Day 8

after irradiation, survival fractions (SF) were assessed using the CellTiter-Glo for 2D and 3D, respectively, as described above.

The dose enhancement factor (DEF<sub>xGy</sub>),<sup>[54]</sup> dose modifying ratio (DMR<sub>xGy</sub>),<sup>[54]</sup> and lethal dose 50% (LD<sub>50%</sub>)<sup>[54]</sup> were calculated as follows:

$$\text{DEF}_{xGy} = \frac{xGy_{\text{control}}}{Gy_{\text{sample required for identical SF}}} \quad (1)$$

with xGy denoting the specific irradiation dose the DEF must be calculated for, xGy<sub>control</sub> the SF of the particle-free control at the given irradiation dose, and Gy<sub>sample</sub> required for identical SF as the respectively required irradiation dose needed to reach the same SF.

$$\text{DMR}_{ySF} = \frac{xGy_{nRE \text{ at } ySF}}{xGy_{ySF}} \quad (2)$$

with ySF denoting a specific SF the DMR is desired to be calculated for, xGy<sub>ySF</sub> the irradiation dose needed for specific SF, and xGy<sub>nRE at ySF</sub> the irradiation dose needed in the nRE-treated sample for a specific SF.

$$\text{LD}_{50} = xGy_{50\% \text{ SF}} \quad (3)$$

with xGy<sub>50% SF</sub> denoting the specific irradiation dose needed to reach 50% of the SF in comparison to the unirradiated sample control.

For comparison, the radiation enhancement factor (RER<sub>xGy</sub>)<sup>[54]</sup> in the same cases was calculated as follows:

$$\text{RER}_{xGy} = \frac{SF_{xGy}}{SF_{nRE \text{ with } xGy}} \quad (4)$$

with xGy as described above, SF<sub>xGy</sub> denoting the SF at specific irradiation dose for particle-free control, and SF<sub>nRE with xGy</sub> denoting the respective SF at a specific irradiation dose for the nRE-treated sample.

**Statistical Analysis:** Data are presented as mean  $\pm$  standard deviation (SD) unless otherwise stated. Sample sizes (N indicates technical repeats, n indicates independent experiments) are indicated in the figure captions. Data analysis was performed in Origin Pro.

## Supporting Information

Supporting Information is available from the Wiley Online Library or from the author.

## Acknowledgements

This project was in part supported by the Gebauer Foundation, the OPO Foundation, the Swiss National Science Foundation (Eccellenza grant number 181290), the Swiss Cancer Research Foundation (KFS-4868-08-2019), and an ETH Grant (ETH-07 21–2). The authors acknowledge the Empa X-ray center for access to their irradiation facilities. Schematics were prepared using BioRender.com.

Open access funding provided by Eidgenössische Technische Hochschule Zurich.

## Conflict of Interest

The authors declare no conflict of interest.

## Data Availability Statement

The data that support the findings of this study are available in the supplementary material of this article.

## Keywords

co-cultured tumor models, metal–organic frameworks, nanoparticles, radio enhancement, radiotherapy

Received: February 14, 2023

Revised: April 11, 2023

Published online: May 13, 2023

- [1] D. Howard, S. Sebastian, Q. V.-C. Le, B. Thierry, I. Kempson, *Iran. J. Med. Sci.* **2020**, 21, 579.
- [2] C. K. Glide-Hurst, I. J. Chetty, *J. Thorac. Dis.* **2014**, 6, 303.
- [3] D. Peukert, I. Kempson, M. Douglass, E. Bezak, *Med. Phys.* **2020**, 47, 651.
- [4] Z. Kuncic, S. Lacombe, *Phys. Med. Biol.* **2018**, 63, 02TR01.
- [5] J. F. Hainfeld, D. N. Slatkin, H. M. Smilowitz, *Phys. Med. Biol.* **2004**, 49, N309.
- [6] C. Bilynsky, N. Millot, A.-L. Papa, *Bioeng. Transl. Med.* **2022**, 7, e10256.
- [7] Y. Imamura, T. Mukohara, Y. Shimono, Y. Funakoshi, N. Chayahara, M. Toyoda, N. Kiyota, S. Takao, S. Kono, T. Nakatsura, H. Minami, *Oncol. Rep.* **2015**, 33, 1837.
- [8] M. Chatzinikolaïdou, *Drug Discovery Today* **2016**, 21, 1553.
- [9] E. C. Costa, A. F. Moreira, D. de Melo-Diogo, V. M. Gaspar, M. P. Carvalho, I. J. Correia, *Biotechnol. Adv.* **2016**, 34, 1427.
- [10] A. G. Souza, I. Beatriz, B. Silva, E. Campos-Fernandez, L. S. Barcelos, J. B. Souza, K. Marangoni, L. R. Goulart, V. Alonso-Goulart, *CPD* **2018**, 24, 1689.
- [11] V. Brancato, F. Gioiella, G. Imparato, D. Guarnieri, F. Urciuolo, P. A. Netti, *Acta Biomater.* **2018**, 75, 200.
- [12] F. Shan, D. A. Close, D. P. Camarco, P. A. Johnston, *Assay Drug Dev. Technol.* **2018**, 16, 27.
- [13] N. Tasdemir, E. A. Bossart, Z. Li, L. Zhu, M. J. Sikora, K. M. Levine, B. M. Jacobsen, G. C. Tseng, N. E. Davidson, S. Oesterreich, *Cancer Res.* **2018**, 78, 6209.
- [14] A. S. Nunes, A. S. Barros, E. C. Costa, A. F. Moreira, I. J. Correia, *Biotechnol. Bioeng.* **2019**, 116, 206.
- [15] L. H. Gray, A. D. Conger, M. Ebert, S. Hornsey, O. C. A. Scott, *Bone Joint Res.* **1953**, 26, 638.
- [16] D. R. Grimes, M. Partridge, *Biomed. Phys. Eng. Express* **2015**, 1, 045209.
- [17] C. Jensen, Y. Teng, *Front. Mol. Biosci.* **2020**, 7, 33.
- [18] B. Pinto, A. C. Henriques, P. M. A. Silva, H. Bousbaa, *Pharmaceutics* **2020**, 12, 1186.
- [19] N. M. Anderson, M. C. Simon, *Curr. Biol.* **2020**, 30, R921.
- [20] B. Arneith, *Medicina* **2019**, 56, 15.
- [21] C. Frantz, K. M. Stewart, V. M. Weaver, *J. Cell Sci.* **2010**, 123, 4195.
- [22] Y.-C. Tung, A. Y. Hsiao, S. G. Allen, Y. Torisawa, M. Ho, S. Takayama, *Analyst* **2011**, 136, 473.
- [23] S. J. Han, S. Kwon, K. S. Kim, *Cancer Cell Int.* **2021**, 21, 152.
- [24] M. Hofer, M. P. Lutolf, *Nat. Rev. Mater.* **2021**, 6, 402.
- [25] R. J. Porter, G. I. Murray, M. H. McLean, *Br. J. Cancer* **2020**, 123, 1209.
- [26] T. H. Booi, C. M. Cattaneo, C. K. Hirt, *Cells* **2022**, 11, 3440.
- [27] C. Jubelin, J. Muñoz-Garcia, L. Griscom, D. Cochonneau, E. Ollivier, M.-F. Heymann, F. M. Vallette, L. Oliver, D. Heymann, *Cell Biosci.* **2022**, 12, 155.
- [28] S. S. Rao, J. DeJesus, A. R. Short, J. J. Otero, A. Sarkar, J. O. Winter, *ACS Appl. Mater. Interfaces* **2013**, 5, 9276.
- [29] Z. Weydert, M. Lal-Nag, L. Mathews-Greiner, C. Thiel, H. Cordes, L. Küpfer, P. Guye, J. M. Kelm, M. Ferrer, *SLAS Discovery* **2020**, 25, 265.
- [30] A. Neuer, L. Gerken, K. Keevend, A. Gogos, I. K. Herrmann, *Nanoscale Adv.* **2020**, 2, 2992.
- [31] M. Rimann, B. Angres, I. Patocchi-Tenzer, S. Braum, U. Graf-Hausner, *SLAS Technol.* **2014**, 19, 191.
- [32] L. R. H. Gerken, A. L. Neuer, P. M. Gschwend, K. Keevend, A. Gogos, A. H. C. Anthis, L. Aengenheister, S. E. Pratsinis, L. Plasswilm, I. K. Herrmann, *Chem. Mater.* **2021**, 33, 3098.
- [33] G. Liu, W. Rui, X. Zhao, X. Lin, *Cell Mol. Immunol.* **2021**, 18, 1085.
- [34] E. Curcio, S. Salerno, G. Barbieri, L. De Bartolo, E. Drioli, A. Bader, *Biomaterials* **2007**, 28, 5487.
- [35] M. Millard, I. Yakavets, V. Zorin, A. Kulmukhamedova, S. Marchal, L. Bezdetnaya, *Int. J. Nanomed.* **2017**, 12, 7993.
- [36] A. Asthana, W. S. Kisaalita, *Drug Discovery Today* **2012**, 17, 810.
- [37] L. G. Griffith, M. A. Swartz, *Nat. Rev. Mol. Cell Biol.* **2006**, 7, 211.
- [38] U. Ziegler, P. Groscurth, *Physiology* **2004**, 19, 124.
- [39] A. L. Neuer, A. Jessernig, L. R. H. Gerken, A. Gogos, F. H. L. Starsich, A. H. C. Anthis, I. K. Herrmann, *Biomater. Sci.* **2022**, 10, 6558.
- [40] J. Marill, N. M. Anesary, P. Zhang, S. Vivet, E. Borghi, L. Levy, A. Pottier, *Radiat. Oncol.* **2014**, 9, 150.
- [41] D. Pan, Y. Chen, Y. Du, Z. Ren, X. Li, B. Hu, *OncoTargets Ther.* **2016**, 8, 4422.
- [42] S. Hehlhans, I. Eke, K. Storch, M. Haase, G. B. Baretton, N. Cordes, *Radiother. Oncol.* **2009**, 92, 362.
- [43] S. Hehlhans, I. Lange, I. Eke, N. Cordes, *Radiother. Oncol.* **2009**, 92, 371.
- [44] K. Storch, I. Eke, K. Borgmann, M. Krause, C. Richter, K. Becker, E. Schröck, N. Cordes, *Cancer Res.* **2010**, 70, 3925.
- [45] H. A. Bicalho, V. Quezada-Novoa, A. J. Howarth, *Chem. Phys. Rev.* **2021**, 2, 041301.
- [46] L. Shukla, R. Luwor, M. E. Ritchie, S. Akbarzadeh, H.-J. Zhu, W. Morrison, T. Karnezis, R. Shayan, *Plast. Reconstr. Surg. Glob. Open* **2020**, 8, e2706.
- [47] L. Maggiorella, G. Barouch, C. Devaux, A. Pottier, E. Deutsch, J. Bourhis, E. Borghi, L. Levy, *Future Oncol.* **2012**, 8, 1167.
- [48] P. L. Olive, R. E. Durand, *Cancer Metastasis Rev.* **1994**, 13, 121.
- [49] L. E. Jamieson, D. J. Harrison, C. J. Campbell, *Analyst* **2015**, 140, 3910.
- [50] G. G. Steel, T. J. McMillan, J. H. Peacock, *Int. J. Radiat. Biol.* **1989**, 56, 1045.
- [51] K. Graham, E. Unger, *Int. J. Nanomed.* **2018**, 13, 6049.
- [52] Promega Corporation · 2800 Woods Hollow Road · Madison, WI 53711–5399 USA.
- [53] T. Kumer, P. K. Das, R. Khatun, M. A. Rahman, S. Akter, S. K. Roy, *Int. J. Med. Phys. Clin. Eng. Radiat. Oncol.* **2021**, 10, 169.
- [54] A. Subiel, R. Ashmore, G. Schettino, *Theranostics* **2016**, 6, 1651.